SOURCE MODEL AND STRONG GROUND MOTION SIMULATION FOR THE 2018 HOKKAIDO EASTERN IBURI, JAPAN, EARTHQUAKE

K. Somei[1], K. Miyakoshi[2], Y. Guo[3]

[1] *Research Associate, Geo-Research Institute, somei@geor.or.jp*
[2] *Chief Researcher, Geo-Research Institute, ken@geor.or.jp*
[3] *Research Associate, Geo-Research Institute, guo@geor.or.jp*

Abstract

The 2018 Hokkaido Eastern Iburi, Japan, earthquake (M_w 6.6) occurred at a deep depth in western part of the Hidaka arc-arc collision zone, and caused strong ground motions with a maximum seismic intensity of 7 in the JMA scale and a maximum peak ground acceleration of over 1000 cm/s^2. In order to understand the mechanisms of generating the broadband strong ground motions during this earthquake, we estimate the spatio-temporal source rupture process based on the waveform inversion using strong motion data, and also construct the characterized source model consisting of Strong Motion Generation Areas (SMGAs) through the broadband ground motion simulations around the source area. To reveal the rupture process, we employ the multi-time window linear waveform inversion by using the strong motion waveforms (0.05-0.5 Hz) recorded around the source area. A curved source fault with a variation in strike angle is assumed by referring the relocated aftershock distribution. The theoretical Green's function is computed assuming a 1D velocity structure model for each station. The SMGAs are estimated on the basis of forward ground motion simulation in broadband frequency range from 0.2 to 10 Hz using the empirical Green's function method. As a result of these source models and ground motion simulation, we concluded the followings. 1) The large slip area (i.e., the asperity area) identified at the depth shallower from the hypocenter, which coincides with the position of the SMGA1, ruptured to up-dip direction and generated the first large broadband ground motions observed at near-source stations. 2) The SMGA2 and 3 played a key role to generate the later phases in the observed waveforms, that is not explained enough only by the SMGA1 or asperity area. 3) The estimated stress drop or short-period level, which control the high-frequency ground motion radiations, were larger than that expected by the average value of past large crustal earthquakes usually occurring in Japan. These findings are important to understand the source characteristics of the earthquakes occurring at deep depth in arc-arc collision tectonic zone.

Keywords: The 2018 Hokkaido Eastern Iburi earthquake, Source model, Strong ground motion

1b-0012

1. Introduction

At 03:08 on 6 September 2018 (Japan Standard Time: JST=UT+9), the 2018 Hokkaido Eastern Iburi earthquake with a magnitude of 6.7 estimated by Japan Meteorological Agency (JMA) occurred in the central Hokkaido, Japan. According to the moment tensor solution released by the F-net broadband seismograph network, which is operated by National Institute of Earth Science and Disaster Resilience, Japan (NIED) [1], this earthquake was an east-dipping reverse faulting with a moment magnitude (M_w) of 6.6 (Fig. 1). JMA unified hypocenter catalogue published the hypocentral depth of this event is 37 km. This is an anomalous depth in contrast to the usual depth around 10 km for crustal earthquakes in Japan. Several studies showed this earthquake occurred beneath the western part of the Hidaka arc-arc collision zone [2, 3]. There have been also some large earthquakes occurring at deep depth around 40-50 km in this region (e.g., M_{JMA}6.7 Hidaka earthquake at depth of 55 km on January 21, 1970, M_{JMA}7.1 Urakawa-oki earthquake at depth of 40 km on March 21, 1982).
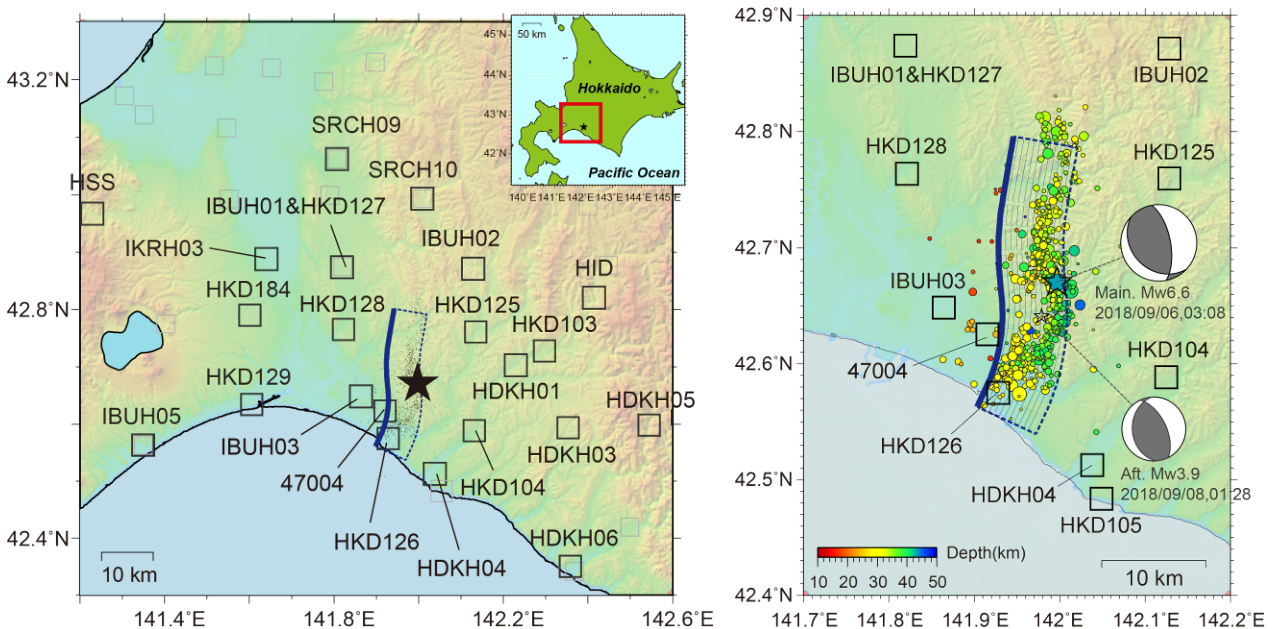

Fig. 1 – Left) Map showing the locations of the stations used in this study (open squares). The gray star indicates the epicenter of the mainshock. The blue curved rectangle represents the map projection of the assumed fault model for the source inversion. Right) Color circles show the aftershock distributions within 12 h after occurring the mainshock. The stars indicate the epicenters of the mainshock and aftershock, which is used as empirical Green's function, with their moment tensor solutions released by F-net, respectively.

The Fire and Disaster Management Agency (2018) [4] reported the 2018 Hokkaido Eastern Iburi earthquake caused severe damage, killing 43 people including related death, injuring 782 others, and completely collapsing 469 buildings in Hokkaido. From the dense nationwide digital strong motion seismograph networks, K-NET, KiK-net [5], F-net [1], installed and operated by the NIED, and seismic intensity observation networks operated by JMA [6], extremely large ground motions with seismic intensity of 7 (or equal to 7) in JMA scale were observed at 47004 (JMA Shikanuma) in Atsuma town and IBUH01 (KiK-net Oiwake) in Abira town. Both IBUH01 and HKD127 (K-NET Oiwake) recorded large maximum peak ground accelerations (PGAs) greater than 1000 cm/s². Takai et al. (2019) [7] focused on the large ground motion with a maximum peak ground velocity (PGV) greater than 100 cm/s recorded around HKD126 (K-NET Mukawa) in Mukawa town. They showed strong ground motion for the frequency range in 0.5–1.0 Hz, which is important to building damage, is mainly amplified by the shallow underground velocity

structure. Dhakal et al. (2019) [8] found that several stations around the source area experienced the non-linear site responses due to the large intensities during the mainshock. They pointed out these non-linear site effects made records increasing in amplification at lower frequency range in relation to the linear case.

In order to elucidate the physical mechanisms of the ground motion generation processes during the 2018 Hokkaido Eastern Iburi earthquake, kinematic heterogeneous slip histories of the source faults have been estimated in space and in time using inversion analyses of strong motion data [9]; both geodetic and strong motion data [10]. These studies used the ground motion data in the frequency range lower than 0.5 Hz. To account for observed strong ground motions in a broadband frequency range, including higher than 0.5 Hz, which are indispensable in terms of seismic damage on buildings and civil structures, a source model consisting of Strong Motion Generation Areas (SMGAs) [11] was also modeled through the forward ground motion simulations [12]. The source models as introduced above showed significant slip area and SMGA are identified to shallower depth relative to the hypocentral depth. Since there is not much knowledges earthquakes occurring arc-arc collision zone, it is still of great importance to comprehensively understand the strong motion generation process in both low and high frequency ranges, as well as how difference the source characteristic between the 2018 Hokkaido Eastern Iburi earthquake and past usual crustal earthquakes. In this study, we deduce both the source rupture process using kinematic inversion analysis in 0.05–0.5 Hz and SMGAs using empirical Green's function method [13] in 0.2–10 Hz, and then discuss the broadband ground motion generation process and source characteristics of this earthquake.

2. Kinematic source inversion

2.1 Source fault setting

The hypocenters of the mainshock and aftershocks are relocated by the double-difference (DD) method [14]. We use P- and S-wave arrival times picked by JMA and the 1D velocity structure model of JMA2001 [15]. Fig. 2 shows the relocated hypocentral distribution for the mainshock and the aftershocks occurring within 12 h after the mainshock. The map view of the relocated aftershock distribution shows the complex shape of the source fault for the mainshock, which is not a single planar fault. Although the whole source fault is east dipping without an obvious variation in dip angle, the strike angle clearly changes between NNW-SSE and NNE-SSW directions. Accordingly, for source inversion, we assumed the *S-shaped* curved fault model with a variation of strike angle from N355°E to N20°E and dip angle of 75° to explain the relocated aftershock distribution.

2.2 Data

In the source inversion analysis, the three-component strong motion records observed at 15 stations of KiK-net and F-net were used (Table 1, Fig. 1). For the KiK-net stations, we used acceleration time histories recorded by downhole strong motion sensors. For the F-net stations, we used velocity time histories recorded by strong motion seismographs. The strong motion station of 47004 located in Atsuma town, which is close to the source fault, recorded acceleration time history. We used horizontal two-component records at IBUH03 because up-down component seismographs in downhole sensor were broken at the station. The observed acceleration waveforms of KiK-net stations were numerically integrated into velocity waveforms in the time domain. All waveform data originally sampled at 100 Hz were band-pass filtered between 0.05 and 0.5 Hz using a sixth-order Chebyshev Type 1 recursive filter with zero-point shift and resampled at 5 Hz. The time durations of 35 s beginning from 1 s prior to the direct S-wave onset were used.

2.3 Theoretical Green's function

The theoretical Green's functions were calculated using the discrete wavenumber method [16] with the reflection and transmission matrix method [17]. Since the difference in velocity structure models among strong motion stations is substantial to prepare reliable Green's functions, a different 1D velocity structure model was constructed for each station, extracting from the nation-wide 3D (three-dimensional) Japan Integrated Velocity Structure Model (JIVSM) [18]. For the three near-source stations (HDKH04, IBUH03,

3

and IKRH03), we used the 1D velocity structure models tuned by integrating the geophysical exploration techniques such as microtremor array analyses, single-station microtremor H/V (horizontal to vertical) spectral ratios, receiver function analyses, and ground motion simulation for a small earthquake [19. 20], in order to prepare the precise Green's function.

Table 1 – Station list used in this study

Station code	Latitude (°N: WGS)	Longitude (°E: WGS)	Location	Network	*1	*2	*3	*4
HDKH01	42.7031	142.2296	Biratori-W	KiK-net	○	○	○	○
HDKH03	42.5934	142.3521	Mombetsu-E	KiK-net	○			
HDKH04	42.5126	142.0381	Mombetsu-W	KiK-net	○		○	○
HDKH05	42.5977	142.5446	Niikappu	KiK-net	○			
HDKH06	42.3498	142.3572	Shizunai	KiK-net	○			
IBUH01	42.8739	141.8191	Oiwake	KiK-net	○	○	○	○
IBUH02	42.8714	142.1285	Hobetsu	KiK-net	○	○	○	○
IBUH03	42.6486	141.8641	Atsuma	KiK-net	○	○	○	○
IBUH05	42.5629	141.3497	Shiraoi	KiK-net	○			
IBUH06	42.4116	141.0017	Muroran	KiK-net	○			
IKRH03	42.8880	141.6399	Chitose	KiK-net	○		○	○
SRCH09	43.0587	141.8063	Kuriyama	KiK-net	○			
SRCH10	43.9930	142.0085	Yubari	KiK-net	○			○
HKD103	42.7275	142.2973	Horokeshi	K-NET				○
HKD104	42.5886	142.1310	Biratori	K-NET				○
HKD125	42.7608	142.1346	Hobetsu	K-NET				○
HKD126	42.5750	141.9279	Mukawa	K-NET				○
HKD127	42.8741	141.8204	Oiwake	K-NET				○
HKD128	42.7655	141.8221	Hayakita	K-NET				○
HKD129	42.6344	141.6057	Tomakomai	K-NET				○
HKD184	42.7900	141.6010	Chitose	K-NET				○
HID	42.8208	142.4145	Hidaka	F-net	○		○	○
HSS	42.9672	141.2286	Sapporo	F-net	○			○
47004	42.6226	141.9204	Shikanuma	JMA				○

Stations used for *1 Source inversion, *2 picking up the S-wave onset data for each SMGA, *3 grid searching for modeling the parameters of SMGA1, and *4 forward ground motion simulations.
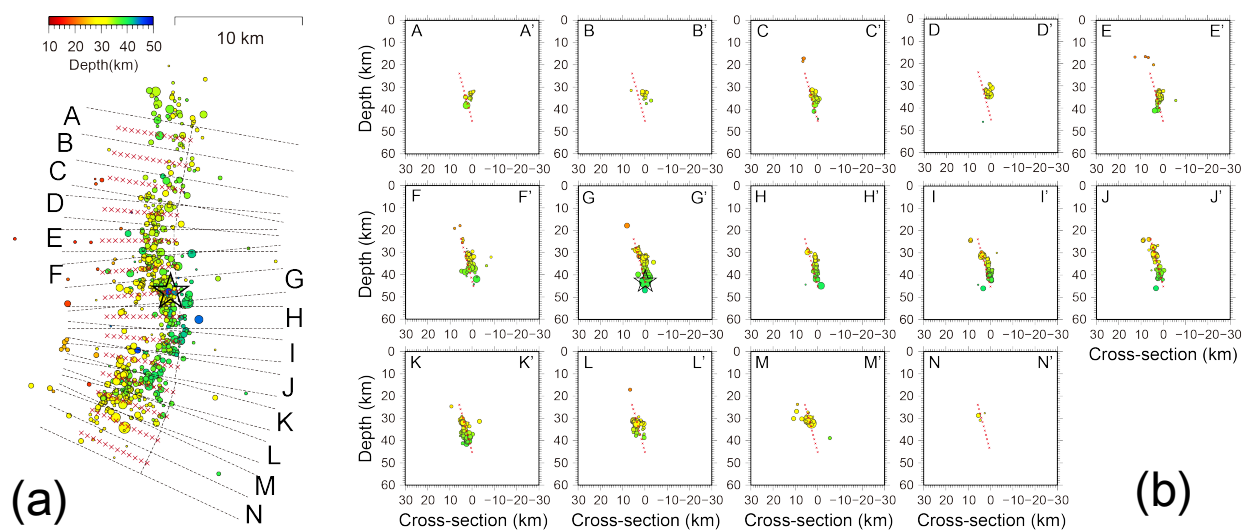

Fig. 2 – Relocated aftershock distributions from 03:07 Sept. 6, 2018 to 15:07 Sept. 6, 2018. The star denotes the hypocenter of the mainshock. Red dots represent the center points of sub-faults assumed in the source inversion analysis. a) Map view. b) The depth section for each box shown in Fig. 2a. X and X' mean the west and east side for each cross section, respectively.

2.4 Finite source inversion method

The spatio-temporal slip history of the 2018 Hokkaido Eastern Iburi earthquake was estimated by the multiple time-window linear waveform inversion method [21, 22]. The observational equation was based on the representation theorem [23, 24] and was discretized in space and time. In this study, the curved fault model was divided into 14 and 12 squared 2 × 2 km subfaults along the strike and dip directions, respectively, meaning the fault length and width are 28 and 24 km, respectively. The rupture starting point was fixed to the relocated hypocenter of the mainshock, which is 42.6703°N, 141.9968°E, at a depth of 43.23 km. The temporal moment-release history at the center of each subfault was represented by five smoothed ramp functions with a time interval of 0.6 s, and a duration of 1.2 s. The first time-window rupture propagation velocity with a constant speed (V_{FT}) was set to 1.6 km/s, which gave the smallest misfit case among the solutions using V_{FT}'s ranging from 1.4 to 3.2 km/s. The rake angle variation was limited within a range in 90° ± 45°. The problem could be solved using the linear least-squares method with a nonnegative constraint [25]. A spatio-temporal smoothing constraint was included following Sekiguchi et al. (2000) [26] to stabilize the solution. A relative weight of the smoothing constraint equation against the observational equation was determined to minimize the Akaike's Bayesian information criterion (ABIC) [27].

2.5 Results and discussion

The slip distributions on the map view and assumed source fault are shown in Fig. 3. The estimated total seismic moment is $1.63×10^{19}$ Nm (M_w 6.74), which is 163% of the seismic moment released by F-net ($1.00×10^{19}$ Nm). The average slip amount over the fault is approximately 0.82 m. A significant slip area with a maximum slip amount of 2.82 m is detected in the depth from 27 to 37 km, which is shallow part from the hypocenter. Whereas, the large slip areas are spread in the depth between 20 and 30 km in the other source inversion result for this event [9, 10]. However, relative differences of depths between the hypocenter and large slip area are comparable each other because the hypocentral depth in this study is deeper than that used in the other study as introduced above. Most aftershocks occurring in the first 12 h after the mainshock are located surrounding the large slip area.

Fig. 4 shows a rupture process snapshot at every 2 s on map view. In the first 6 s, small slip rupture propagated from the hypocenter. Then, the main rupture grew up to upward direction, and significant large slip area was ruptured from 6 to 10 s. The entire rupture finished within 18 s. Fig. 3c also shows an asperity area extracted by the criteria of Somerville et al. (1999) [28], whose size is 128 km² including the significant large slip area. As shown in Fig. 5, the synthesized velocity waveforms fit the observed ones well, although some discrepancies still remain. The observed waveforms for most stations are explained by the synthetics generated from the asperity area. In particular, the large pulse observed at near-source stations (e.g., IBUH01, IBUH03) are mainly contributed by the asperity area.

3. Strong motion generation areas and ground motion simulation

3.1 Empirical Green's function method

As stated in introduction, we use the empirical Green's function (EGF) method [13] to simulate the ground motions over a wide frequency range. The EGF method is a technique used to synthesize seismic records for large earthquake by summing up the observed records of small earthquakes as empirical Green's functions convolved with a filtering function or correction function, which corrects the difference in the slip velocity time function between the large and small events. In general, calculating a Green's function from source to station, which explains in higher frequency range, is difficult, because we do not know a detailed 3D underground structure. From that point of view, a clear advantage in EGF method is what we directly know the Green's function by using the observed records of small earthquake. Hereafter we call the small earthquake as 'EGF event'.

SMGA is the characterized source patch model with a large uniform slip velocity inside the total rupture area, which reproduce strong ground motions up to 10 Hz [11]. Broadband ground motions observed

5

1b-0012

in past large earthquakes have been successfully simulated by EGF method and SMGA models [29, 30, 31]. For modeling the SMGA of the 2018 Hokkaido Eastern Iburi earthquake, we used the records of an M_w 3.9 aftershock as an EGF event whose source parameters are listed together with those of the mainshock in Table 2. This EGF event had a similar focal mechanism to that of the mainshock and occurred close to the hypocenter of the mainshock (Fig. 1).

3.2 Rupture starting points of SMGAs

Since the three S-wave packets (S1–S3) were observed at near-source stations, we assumed three squared SMGAs on the curved source fault using in source inversion analysis. The location of rupture starting point and rupture time for each SMGA were objectively determined by following the method proposed by Asano and Iwata (2012) [30], that is based on the observed and theoretical travel time for each S-wave packet. The observed S-wave onset data at four stations listed in Table 1 were used. To calculate the theoretical S-wave travel time, here we used a 1D velocity structure model extracted from the JIVSM [18] at the epicenter of the mainshock. Fig. 6 shows the estimated rupture starting points of three SMGAs on the source fault. The rupture delay times from the origin time are 4.5, 7.0, and 12.0 s, respectively. As seen in Fig. 6, the location of the rupture starting point was well determined along the strike direction although the spatial uncertainty in the dip direction is larger than that in the strike direction.
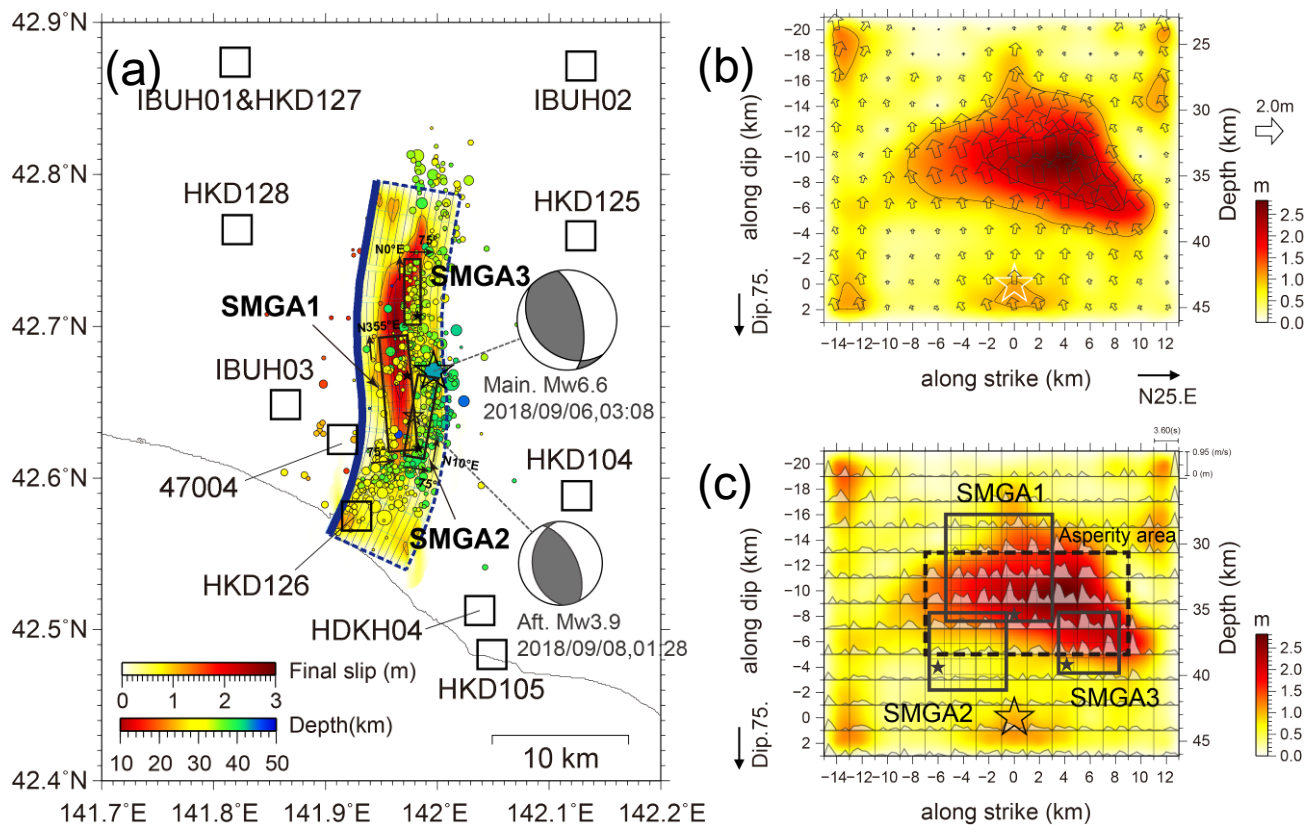

Fig. 3 – a) Final slip distribution and SMGAs projected in map view. Color circles show the aftershock distributions within 12 h after occurring the mainshock. The stars indicate the epicenters of the mainshock and aftershock, which is used as empirical Green's function, with their moment tensor solutions released by F-net, respectively. b) Final slip distribution on the fault plane with a contour interval of 1 m. The arrows show the slip vectors of the hanging wall relative to the footwall. The open star indicates the hypocenter or the rupture starting point. c) Moment rate functions for each sub-fault. Black dotted and gray rectangles show the asperity area and SMGA, respectively. Solid stars indicate the rupture starting points of SMGAs
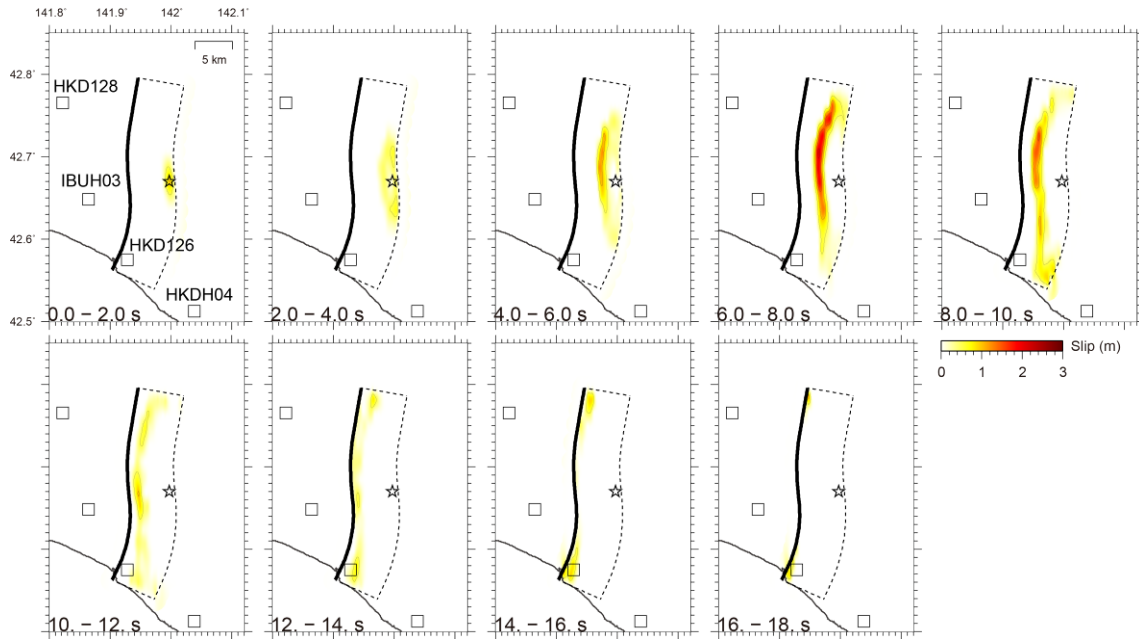
Fig. 4 – Snapshot of the spatio-temporal slip progression at time steps of 2 sec. in map view. The open star indicates the rupture starting point.
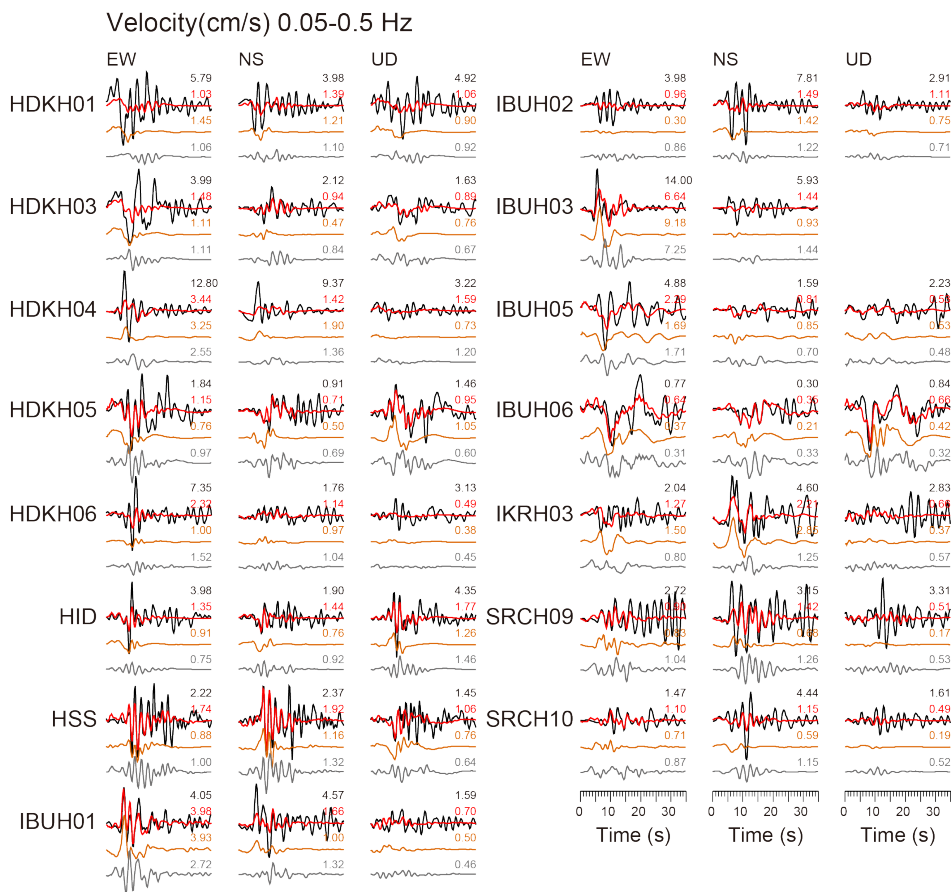

Fig. 5 – Observed (Black) and synthetic velocity waveforms in 0.05–0.5 Hz. Orange and gray indicate the synthetic waveforms generated from the asperity area and off asperity area, respectively.

7

Table 2 – Source parameters of the mainshock and the EGF event.

	Mainshock	EGF event
Origin time (JST=UT+9) [*1]	6 Sept. 2018, 03:07	7 Sept. 2018, 01:28
Epicentral Latitude[*1]	42.6703°N	42.6656°N
Epicentral Longitude[*1]	141.9968°E	140.9901°E
Hypocentral depth[*1]	43.23 km	35.67 km
Focal mechanism (Strike, Dip, Rake) [*2]	(349, 65, 107)	(334, 59, 78)
Seismic moment (M_w) [*2]	1.00×10^{19} Nm (6.6)	9.41×10^{14} Nm (3.9)

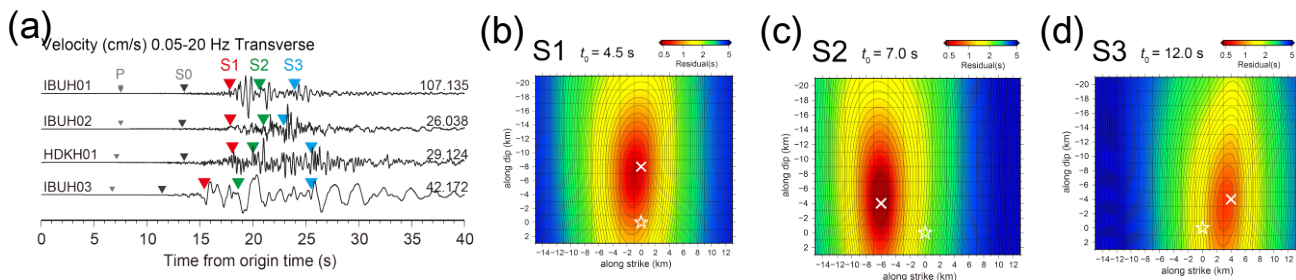[*1] Hypocenter information relocated by DD method, [*2] F-net

Fig. 6 – a) Observed velocty waveforms in Transverse component and the P- and S-wave onsets at four stations. b) For S1, c) S2 and, d) S3, distributions of RMS residual estimated by the grid search method for locating the rupture starting points of SMGAs The cross denotes the minimum value. The hypocenter of the mainshock is indicated by the open star.

3.3 Modeling the SMGA parameters

We performed forward ground motion simulations in the broadband frequency range from 0.2 to 10 Hz, to construct the SMGA model. In the preliminary analysis of strong motion simulation, we found the SMGA1 could explain the largest S-wave packet (S1) in the observed waveforms. Therefore, we first estimate the best set of parameters for SMGA1 using a grid searching, to reproduce the observed waveforms at near-source stations. Four parameters for the SMGA1 representing the size (length and width), position (rupture starting point within SMGA), rise time, and rupture velocity were estimated by minimizing the residuals of both the acceleration envelope and displacement waveform fittings between the observations and simulations for 30 s including the S-wave portions in the three components at six KiK-net and one F-net stations listed in Table 1. The relative rupture starting point within the SMGA1 in dip direction was fixed to the bottom of the SMGA1, considering the rupture propagation from the hypocenter located deeper than the starting point of the SMGA1. The search range, interval, and estimated value of the parameters for the SMGA1 are listed in Table 3. Then, the parameters of SMGA2 and 3 are determined by the trial and error process to compensate the remained S2 and S3 packets in observed waveforms as fixing the parameter of SMGA1.

Table 3 – Search range, interval, and estimated value of parameters for SMGA1 in the grid search.

SMGA1		Search range	Interval	Estimated
Length = Width	$L = W$ (km)	4.2–10.5	0.7	8.4
Rise time	τ (s)	0.35–0.77	0.07	0.42
Rupture velocity	V_r (km/s)	1.6–3.4	0.1	2.5
Rupture starting point of SMGA	NSL*	1–7	1	5
	NSW*	7	fixed	7

* NSL and NSW indicate the rupture starting subfault within SMGA in the strike and dip directions.

8

3.4 Results and discussion

The estimated SMGAs for the 2018 Hokkaido Eastern Iburi earthquake are shown in Fig. 3, whose parameters are listed in Table 4. The SMGA1 was located near the large slip area (i.e., asperity area) of the kinematic source model, and its rupture propagated to the up-dip direction. The SMGA2 and 3 were identified to deeper part from the SMGA1 and both ruptures propagated to north and upward direction. Overall, the spatial positions of SMGA1 and 3 coincide with the asperity area although the SMGA2 is not overlapped to the asperity area or large slips detected by source inversion. However, the time of rupture mostly matches between the SMGA1 and asperity area; the SMGA2 and 3 ruptured at the latter part of whole duration after terminating the rupture of the asperity area. Fig. 7 shows the comparison of velocity waveforms between the observations and simulations. The simulated velocity waveform radiated from the SMGA1 could reproduce well the main pulse or packet (S1) in observation. In particular, the large pulse observed at IBUH03 was generated by the upward rupture directivity effect within the SMGA1. The later phases, which are not produced only from SMGA1, were explained by the simulations of SMGA2 and 3 fairly well (e.g., IBUH01 and IBUH03). Therefore, SMGA2 and 3 are necessary to explain the ground motion generations in the whole source rupture process, which is not clearly found from the observed data in a low frequency range used in source inversion.

The estimated stress drops of SMGAs were 19.1 MPa, which is approximately 1.5 times larger than that expected by the average value of past large crustal earthquakes usually occurring in Japan. The short-period level calculated from the stress drops and the sizes of SMGAs was 2.23×10^{19} Nm/s^2, which is also larger than that expected by the empirical scaling relationship for crustal earthquakes [32] (Fig. 8). This large short-period level of the mainshock was also shown by the spectral inversion analyses applied to the 2018 Hokkaido Eastern Iburi earthquake sequence [33, 34]. These findings are important to understand the source characteristics of the earthquakes occurring at deep depth in arc-arc collision tectonic zone.

Table 4 – Estimated parameters of the SMGAs.

		SMGA1	SMGA2	SMGA3
Length	L (km)	8.4	6.0	4.8
Width	W (km)	8.4	6.0	4.8
Area	S (km^2)	70.6	36.0	23.0
Rise time	τ (s)	0.42	0.50	0.60
Seismic moment	M_0 (Nm)	4.64×10^{18}	1.69×10^{18}	8.67×10^{17}
Moment magnitude	M_w	6.38	6.09	5.89
Stress drop	$\Delta\sigma$ (MPa)	19.1	19.1	19.1
Rupture velocity	V_r (km/s)	2.5	2.5	2.5
Rupture delay time	T_{delay} (s)	+4.5	+7.0	+12.0
Strike, Dip	$Str., Dip.$ (deg.)	355, 75	10, 75	0, 75

4. Conclusions

The source rupture process and SMGAs for the 2018 Hokkaido Eastern Iburi earthquake were inferred from the observed strong motion data. On the basis of the relocated aftershock distribution, the curved source fault model with a variation in strike angle was assumed to estimate the source model. Target frequency ranges are 0.05–0.5 and 0.2–10 Hz for source inversion and SMGA modeling, respectively. The principal findings were as follows. 1) The large slip area (i.e., the asperity area) identified at the depth shallower from the hypocenter, which coincides with the position of the SMGA1, ruptured to up-dip direction and generated the first large broadband ground motions observed at near-source stations. 2) The SMGA2 and 3 played a key role to generate the later phases in the observed waveforms, that is not explained enough only by the SMGA1 or asperity area. 3) The estimated stress drop or short-period level, which control the high-frequency ground motion radiations, were larger than that expected by the average value of past large crustal earthquakes usually occurring in Japan.
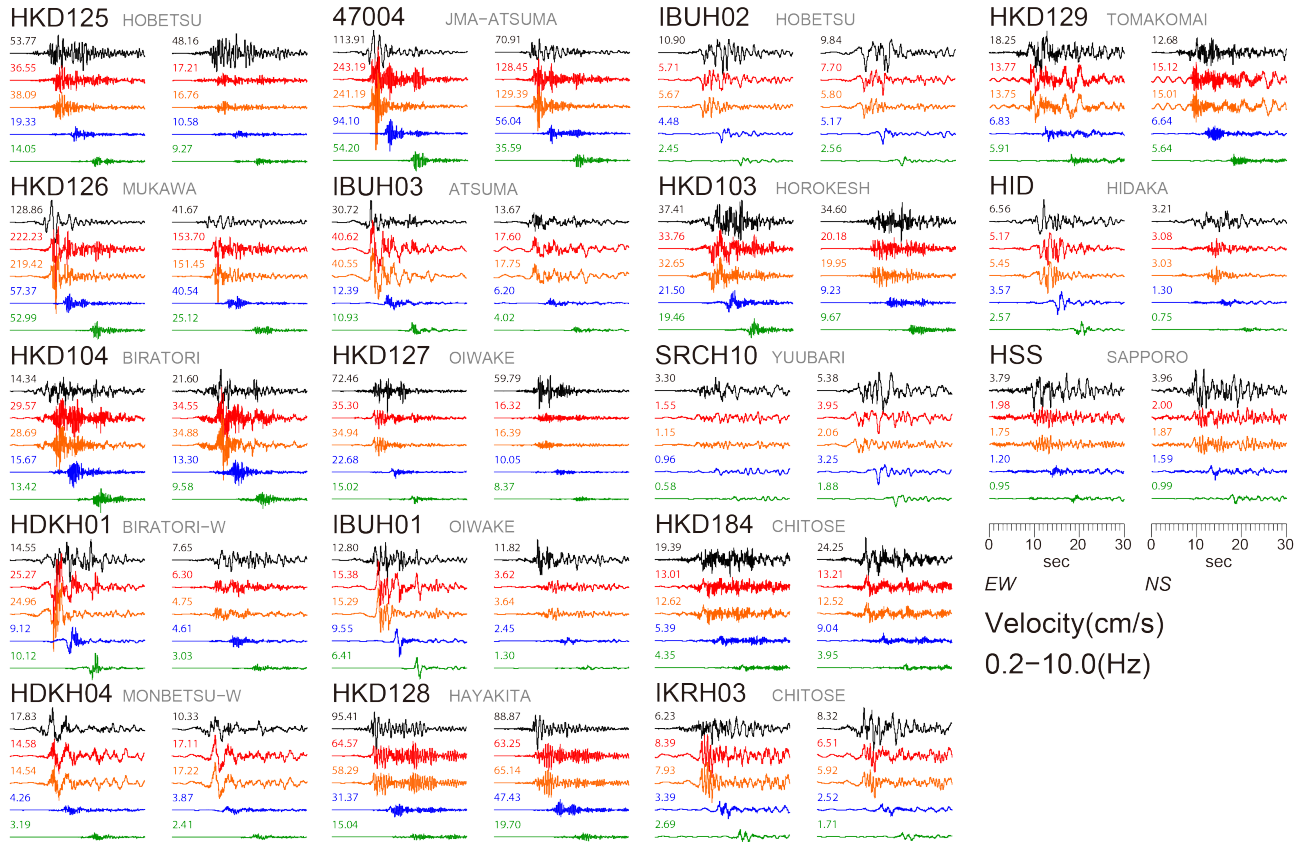
Fig. 7 – Observed (Black) and simulated (Red) velocity waveforms in 0.2-10 Hz. Orange, blue, and green represent the simulations generated from each SMGA1, 2, and 3, respectively.
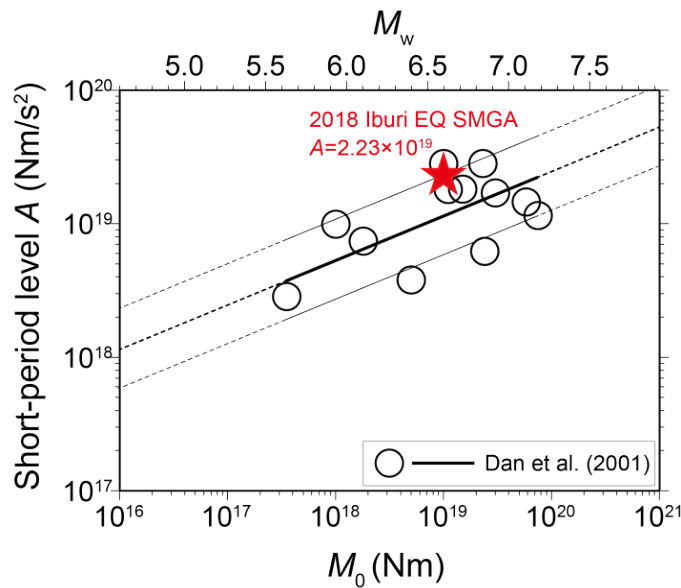

Fig. 8 – Relationship between short-period level A and seismic moment M_0.

10

1b-0012

5. Acknowledgements

6. References

[1] National Research Institute for Earth Science and Disaster Resilience (2019): NIED F-net, National Research Institute for Earth Science and Disaster Resilience, https://doi.org/10.17598/NIED.0005.

[2] Iwasaki T, Tsumura N, Ito T, Arita K, Matsubara M, Sato H, Kurashiro E, Hirata N, Abe S, Noda K, Fujiwara A, Kikuchi S, Suzuki K (2019): Structural heterogeneity in and around the fold-and-thrust belt of the Hidaka Collision zone, Hokkaido, Japan and its relationship to the aftershock activity of the 2018 Hokkaido Eastern Iburi Earthquake, *Earth, Planets and Space*, **71**:103, https://doi.org/10.1186/s40623-019-1081-z.

[3] Kita S (2019): Characteristics of relocated hypocenters of the 2018 M6.7 Hokkaido Eastern Iburi earthquake and its aftershocks with a three-dimensional seismic velocity structure, *Earth, Planets and Space*, **71**:122, https://doi.org/10.1186/s40623-019-1100-0.

[4] Fire and Disaster Management Agency (2018): The 2018 Hokkaido Eastern Iburi earthquake (35th report), https://www.fdma.go.jp/disaster/info/items/b3ad91b60531fcb1854a444954c7a97a82128a1a.pdf. Accessed 21 Jan. 2020 (in Japanese).

[5] National Research Institute for Earth Science and Disaster Resilience (2019): NIED K-NET, KiK-net, National Research Institute for Earth Science and Disaster Resilience, https://doi.org/10.17598/NIED.0004.

[6] Nishimae Y (2004): Observation of seismic intensity and strong ground motion by Japan Meteorological Agency and local governments in Japan. *Journal of Japan Association for Earthquake Engineering*, **4** (3), 75–78.

[7] Takai N, Shigefuji M, Horita J, Nomoto S, Maeda T, Ichiyanagi M, Takahashi H, Yamanaka H, Chimoto K, Tsuno S, Korenaga M, Yamada N (2019): Cause of destructive strong ground motion within 1–2 s in Mukawa town during the 2018 M_w 6.6 Hokkaido eastern Iburi earthquake, *Earth, Planets and Space*, **71**:67, https://doi.org/10.1186/s40623-019-1044-4.

[8] Dhakal YP, Kunugi T, Kimura T, Suzuki W, Aoi, S (2019): Peak ground motions and characteristics of nonlinear site response during the 2018 Mw 6.6 Hokkaido eastern Iburi earthquake, *Earth, Planets and Space*, **71**:56, https://doi.org/10.1186/s40623-019-1038-2.

[9] Asano K, Iwata T (2019): Source rupture process of the 2018 Hokkaido Eastern Iburi earthquake deduced from strong-motion data considering seismic wave propagation in three-dimensional velocity structure, *Earth, Planets and Space*, **71**:101, https://doi.org/10.1186/s40623-019-1080-0.

[10] Kobayashi H, Koketsu K, Miyake H (2019): Rupture process of the 2018 Hokkaido Eastern Iburi earthquake derived from strong motion and geodetic data, *Earth, Planets and Space*, **71**:63, https://doi.org/10.1186/s40623-019-1041-7.

[11] Miyake H, Iwata T, Irikura K (2003): Source characterization for broadband ground-motion simulation: Kinematic heterogeneous source model and strong motion generation area, *Bulletin of the Seismological Society of America*, **93**, 2531–2545.

[12] Satoh T (2019): Broadband source model and strong motions of the 2018 Hokkaido Eastern Iburi earthquake, *Journal of Structural and Construction Engineering*, **84** (763), 1175–1185.

[13] Irikura K (1986): Prediction of strong acceleration motions using empirical Green's function, *Proceedings of the 7th Japan Earthquake Engineering Symposium, Tokyo*, 151–156.

[14] Waldhauser F, Ellsworth WL (2000): A double-difference earthquake location algorithm: method and application to the Northern Hayward Fault, California, *Bulletin of the Seismological Society of America*, **90**, 1353–1368.

[15] Ueno H, Hatakeyama S, Aketagawa T, Funasaki J, Hamada N (2002): Improvement of hypocenter determination procedures in the Japan Meteorological Agency, *Q J Seismol.*, **65**, 123–134 (in Japanese with English abstract).

[16] Bouchon M (1981): A simple method to calculate Green's function for elastic layered media, *Bulletin of the Seismological Society of America*, **71**, 959–971.

[17] Kennett BLN, Kerry NJ (1979): Seismic waves in a stratified half space, *Geophysical Journal of the Royal Astronomical Society*, **57**, 557–583.

[18] Koketsu K, Miyake H, Suzuki H (2012): Japan integrated velocity structure model version 1, *Proceedings of the 15th world conference on earthquake engineering, Lisbon*, *24–28 September 2012*, Paper No.1773.

[19] Somei, K, Ling S, Miyakoshi K, Yoshida K, Guo Y (2019): Velocity structure around the source area of the 2018 Hokkaido Eastern Iburi earthquake estimated from array and single-station microtremor observations, *Proceedings of the 141st Society of Exploration Geophysicists of Japan Conference, Iwate, 29–31October 2019*, 127-130.

[20] Yoshida K, Miyakoshi K, Somei K, Ling S (2019): Sedimentary basin structure inferred from receiver function analysisat KiK-net sites in Eastern Iburi, Hokkaido, *Proceedings of the 141st Society of Exploration Geophysicists of Japan Conference, Iwate, 29–31October 2019*, 131-134.

[21] Hartzell SH, Heaton T (1983): Inversion of strong ground motion and teleseismic waveform data for the fault rupture history of the 1979 Imperial Valley, California, earthquake. *Bulletin of the Seismological Society of America*, **73**, 1553–1583.

[22] Olson AH, Apsel RJ (1982): Finite faults and inverse theory with applications to the 1979 Imperial Valley earthquake. *Bulletin of the Seismological Society of America*, **72**. 1969–2001.

[23] Maruyama T (1963): On the force equivalents of dynamic elastic dislocations with reference to the earthquake mechanism, *Bulletin of the Earthquake Research Institute, University of Tokyo*, **41**, 467–486.

[24] Burridge R, Knopoff L (1964): Body force equivalents for seismic dislocations, *Bulletin of the Seismological Society of America*, **54**, 1875–1888.

[25] Lawson CL, Hanson RJ (1974): Solving least squares problems. Prentice-Hall, Old Tappan.

[26] Sekiguchi H, Irikura K, Iwata T (2000) Fault geometry at the rupture termination of the 1995 Hyogo-ken Nanbu earthquake, *Bulletin of the Seismological Society of America*, **90**, 117–133.

[27] Akaike H (1980): Likelihood and the Bayes procedure. *Trabajos de Estadistica Y de Investigacion Operativa*, **31**(1), 143–166.

[28] Somerville P, Irikura K, Graves G, Sawada S, Wald D, Abrahamson N, Iwasaki Y, Kagawa T, Smith N, and Kowada A (1999): Characterizing crustal earthquake slip models for the prediction of strong ground motion. *Seismological Research Letter*, **70**, 59–80.

[29] Oth A, Wanzel F, Radulian M (2007): Source parameters of intermediate-depth Vrancea (Romania) earthquakes from empirical Green's functions modeling, *Tectonophysics*, **438**, 33–56

[30] Asano K, Iwata T (2012): Source model for strong ground motion generation in the frequency range 0.1-10 Hz during the 2011 Tohoku earthquake, *Earth Planets Space*, **64**, 1111-1123.

[31] Somei K, Miyakoshi K, Yoshida K, Kurahashi S, Irikura K (2019): Near-Source Strong Pulses During Two Large M_{JMA} 6.5 and M_{JMA} 7.3 Events in the 2016 Kumamoto, Japan, Earthquakes, *Pure and Applied Geophysics*, https://doi.org/10.1007/s00024-019-02095-6.

[32] Dan K, Watanabe M, Sato T, Ishii T (2001): Short-period source spectra inferred from variable-slip rupture models and modeling of earthquake faults for strong motion prediction by semi-empirical method, *Journal of Structural and Construction Engineering*, **545**, 51–62.

[33] Tomozawa Y, Kato K, Nojiri K (2019): Estimation of source, path and site effects of the 2018 Hokkaido Eastern Iburi earthquake, *Journal of Japan Association for Earthquake Engineering*, **19** (4), 4_170–4_174.

[34] Nakano K, Kawase H (2019): Source parameters and site amplifications estimated by generalized inversion technique: focusing on the 2018 Hokkaido Iburi-Tobu earthquake, *Earth, Planets and Space*, **71**:66, https://doi.org/10.1186/s40623-019-1047-1.